Letter

Graph morphology of non-Hermitian bands

Yuncheng Xiong [1] and Haiping Hu [1,2,*]

[1] *Beijing National Laboratory for Condensed Matter Physics, Institute of Physics, Chinese Academy of Sciences, Beijing 100190, China*
[2] *School of Physical Sciences, University of Chinese Academy of Sciences, Beijing 100049, China*

(Received 13 November 2023; revised 22 February 2024; accepted 22 February 2024; published 15 March 2024)

Non-Hermitian systems exhibit diverse graph patterns of energy spectra under open boundary conditions. Here, we present an algebraic framework to comprehensively characterize the spectral geometry and graph topology of non-Bloch bands. Using a locally defined potential function, we unravel the spectral-collapse mechanism from Bloch to non-Bloch bands, delicately placing the spectral graph at the troughs of the potential landscape. The potential formalism deduces the non-Bloch band theory and generates the density of states via the Poisson equation. We further investigate the Euler-graph topology by classifying spectral vertices based on their multiplicities and projections onto the generalized Brillouin zone. Through concrete models, we identify three elementary graph-topology transitions (UVY, $\mathcal{PT}$-like, and self-crossing), accompanied by the emergence of singularities in the generalized Brillouin zone. Lastly, we unveil how to generally account for isolated edge states outside the spectral graph. Our work lays the cornerstone for exploring the versatile spectral geometry and graph topology of non-Hermitian non-Bloch bands.

DOI: 10.1103/PhysRevB.109.L100301

Introduction. Non-Hermiticity emerges as a significant factor in a wide range of classical wave systems and open quantum systems, giving rise to various peculiar properties and applications [1–7]. A distinctive feature of non-Hermitian systems is the non-Hermitian skin effect (NHSE) [8–19], where an extensive number of eigenstates are localized at the system boundaries [20–25]. To accommodate the presence of skin modes, the notion of a generalized Brillouin zone (GBZ) [8] has been introduced by extending the Bloch wave vector to the complex domain. Depending on the boundary conditions, the energy spectra either manifest as closed loops with nontrivial spectral windings, representing Bloch bands under periodic boundary conditions (PBCs), or they adopt open arcs (i.e., non-Bloch bands) on the complex-energy plane under open boundary conditions (OBCs).

A synopsis of earlier non-Hermitian band theory involves symmetry classifications of eigenenergy bands based on point or line gaps [26–30]. A homotopy perspective further distinguishes separable bands by their eigenenergy braidings [31–41]. These classifications, however, are exclusive to Bloch bands. Under OBC, the arc-shaped non-Bloch bands display a plethora of intricate patterns, forming planar graphs on the complex plane [42,43] which are linked to the algebraic properties of characteristic polynomials (ChPs). The primary focuses of the non-Bloch band theory [8–11] have been on producing the continuum of non-Bloch bands and restoring the bulk-edge correspondence via the GBZ. Yet the intricate connections between these two types of spectral patterns (i.e., loops versus graphs), and the physical mechanism governing their transformations remain enigmatic. Recently, the electrostatic analogy [44,45] has been employed to analyze non-Bloch bands, aiding in the determination of spectral patterns and density of states (DOS). Broadly speaking, the intriguing graph geometry goes beyond the scope of conventional topological invariants such as $\mathbb{Z}, \mathbb{Z}_2$ or spectral windings [12,13,46,47]. It represents uncharted band topology which may yield novel non-Bloch symmetries [48,49] and spectral transitions between distinct graph patterns relevant for anomalous responses [42,50]. To date, the non-Bloch bands with respect to their Euler-graph morphology have largely been unexplored, and a systematic classification of their spectral transitions is also lacking.

In this Letter, we present an algebraic framework to comprehensively characterize the graph geometry and topology of one-dimensional non-Hermitian bands. Inspired by the electrostatic analogy [44,45], we unveil the electrostatic mechanism of spectral collapse and reproduce the non-Bloch band theory and the GBZ by incorporating a local potential function $\Phi(E)$. Notably, the potential function is harmonic on the complex plane, except at locations coinciding with spectral graphs, aligning precisely with the troughs of the potential landscape. Furthermore, we delve into the Euler-graph topology and systematically classify the spectral vertices according to their multiplicities and projections onto the GBZ. We demonstrate three elementary graph transitions, as well as the appearance of singularities within the GBZ, and address the treatment of isolated edge modes that exist beyond the continuum of non-Bloch bands.

Spectral collapse. Let us first recap the non-Bloch band theory via the simplest Hatano-Nelson model [51]. The Hamiltonian $H=\sum_j t_L c_j^\dagger c_{j+1} + t_R c_{j+1}^\dagger c_j$ consists of nearest hoppings to the left with strength $t_L > 0$ and to the right with $t_R > 0$, over a total of N lattice sites. As shown in Fig. 1(a), the energy spectra form a closed oval under PBC while residing

*Corresponding author: hhu@iphy.ac.cn

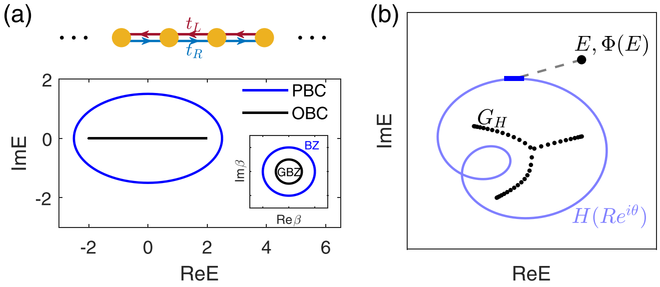

FIG. 1. (a) Top: Schematics of the Hatano-Nelson model with asymmetric hoppings t_R and t_L. Bottom: Energy spectra under PBC (blue) and OBC (black), respectively. $t_L = 2$, $t_R = 0.5$. Inset: loci of the Bloch factor $\beta = e^{ik}$ on the complex plane. (b) Sketch of the electrostatic analogy. By assigning a charge of $1/N$ (N is the system size) to each point on the OBC spectra (black), the Coulomb potential $\Phi(E)$ felt at E equals the electrostatic potential induced by the charged spectral loop described by $H(Re^{i\theta})$ with $\theta \in [0, 2\pi]$. The factor R is chosen such that E is outside the loop.

at the line connecting the two foci of the oval under OBC, $E \in [-2\sqrt{t_R t_L}, 2\sqrt{t_R t_L}]$. Consequently, all N eigenstates are localized at either the left or right boundary depending on the ratio t_L/t_R. In momentum space, the Hamiltonian takes $H(k) = t_L e^{ik} + t_R e^{-ik}$. By substituting $\beta = e^{ik}$, it is easy to see that the eigenstates under OBC are skin modes associated with complex Bloch vectors, i.e., $\beta_m = \sqrt{t_R/t_L} e^{\pm \frac{i2\pi m}{N+1}}$, with m the level index. In the continuum limit $N \to \infty$, all β_m's form a circle of radius $\sqrt{t_R/t_L}$, which is the GBZ of the system.

The elegant spectral collapse into the oval's central axis is no accident. For a generic non-Hermitian Hamiltonian $H(k)$, the OBC energy spectra are determined by the bivariate ChP ($\beta = e^{ik}$),

$$f(E, \beta) = \det(H(\beta) - E) = \sum_{j=-p}^{q} f_j(E) \beta^j. \quad (1)$$

For a given E, we order the solutions of $f(E, \beta) = 0$ as $|\beta_1(E)| \leqslant |\beta_2(E)| \leqslant \cdots \leqslant |\beta_{p+q}(E)|$. In the continuum limit, the OBC spectra (except for a finite number of isolated edge states, if any) reside within the PBC spectral loop and form some Euler graph, denoted as G_H. Any point on the graph satisfies the condition $|\beta_p(E)| = |\beta_{p+1}(E)|$. The locus of β on the complex plane obeying this condition gives the GBZ and traces a closed curve enclosing the origin.

The spectral collapse from PBC to OBC necessitates the point gap. Utilizing the so-called rescaled spectra Sp(R) [13,52] which are the regions enclosed by the spectral loop of $H(Re^{i\theta})$ with $\theta \in [0, 2\pi]$. The graph emerges as the intersection of these rescaled spectra with all feasible rescaling factors R:

$$G_H = \bigcap_{R \in (0,\infty)} \mathrm{Sp}(R). \quad (2)$$

G_H thus obtained is constituted by a collection of arcs [53,54] and connected [55]. Algebraically, the collapse process is captured by an electrostatic analogy [45] which assigns a charge $1/N$ to each eigenvalue E_n ($n = 1, 2, \ldots, N$) of the OBC Hamiltonian. The Coulomb potential at $E \notin G_H$ is $\Phi(E) = \frac{1}{N} \sum_n \log |E_n - E|$. According to Szegö's limit theorem [56,57], the potential $\Phi(E)$ in the continuum limit equals the integral, $\Phi(E) = \frac{1}{2\pi} \int_0^{2\pi} \log |\det[H(Re^{i\theta}) - E]| d\theta$ with $|\beta_p(E)| < R < |\beta_{p+1}(E)|$. Physically, the integral can be interpreted as the Coulomb potential due to the charged spectral loop $H(Re^{i\theta})$ with $\theta \in [0, 2\pi]$, as sketched in Fig. 1(b). For any point $E \notin G_H$, the rescaling factor R always exists.

Spectral graphs. The potential function $\Phi(E)$ is well defined on the complement of the graph G_H. Notably, it can be represented in a compact form [58]:

$$\Phi(E) = \log |f_q(E)| + \sum_{j=p+1}^{p+q} \log |\beta_j(E)|. \quad (3)$$

Thus, Eq. (3) can be straightforwardly continued to the whole complex plane without ambiguity as long as the q roots of the largest moduli in the sum are chosen. The potential $\Phi(E)$ is harmonic outside the graph G_H, i.e., $\nabla_E^2 \Phi(E) = 0$ for $E \notin G_H$. In the distributional sense, the density of states (DOS) in the continuum limit is $\rho(E) = \lim_{N\to\infty} \frac{1}{N} \sum_n \delta_{E,E_n}$. The electrostatic analogy implies that the DOS satisfies the Poisson equation

$$\rho(E) = \frac{1}{2\pi} \nabla_E^2 \Phi(E). \quad (4)$$

Clearly, a nonzero DOS can only be obtained when $E \in G_H$ or $|\beta_p(E)| = |\beta_{p+1}(E)|$, which is exactly the GBZ condition. On the complex-energy plane, the graph G_H resides at the troughs of the potential landscape. The significant benefit of the potential formalism lies in its ability to derive the spectral graph and DOS without solving the GBZ or large OBC Hamiltonians.

We illustrate the potential description with two simple examples. (i) The Hatano-Nelson model: The potential is $\Phi(E) = \frac{1}{2} \log \max(|E \pm \sqrt{E^2 - 4t_R t_L}|)$. Figures 2(a) and 2(c) plot respectively the potential landscape and the DOS after taking the Laplacian on the complex plane. The DOS with respect to arc length [58] is $\frac{d\rho}{dE} = \frac{1}{\pi} \frac{1}{\sqrt{4t_L t_R - E^2}}$, which is divergent at the two endpoints. (ii) $H(\beta) = \beta^2 + \beta^{-1}$: The potential landscape is shown in Fig. 2(b). The OBC spectra form a threefold symmetric fan with three branches: $G_H = \cup_m e^{i\frac{2m\pi}{3}} [0, 3/\sqrt[3]{4}]$ ($m = 0, 1, 2$), joining at the junction point $E = 0$. The DOS with respect to the arc length [58] is $\frac{d\rho}{dE} = \frac{\sqrt{3}}{12\pi} \frac{1}{C_+^2 + C_-^2 - C_+ C_-} (\frac{1}{4} - \frac{|E|^3}{27})^{-1/2}$, with $C_\pm = (-\frac{1}{2} \pm \sqrt{\frac{1}{4} - \frac{|E|^3}{27}})^{1/3}$, as shown in Fig. 2(d). For more complicated cases, the potential function, spectral graph, and DOS can be solved numerically.

Euler-graph topology. The topology of the graph G_H is specified by the number of vertices (n_V), edges (n_E), and faces (n_F). They satisfy the Euler formula [59]

$$n_V - n_E + n_F = 2. \quad (5)$$

For clarity, we also label a graph by $G(n_V, n_E)$ hereafter. Usually, the information of a finite set of points on G_H, e.g., the endpoints and the junction points with their multiplicities, is sufficient to determine the graph topology. These special points can be obtained via fairly simple analytical methods. To this end, we classify the points on the graph by their local geometric structures. Let us take a small circle enclosing

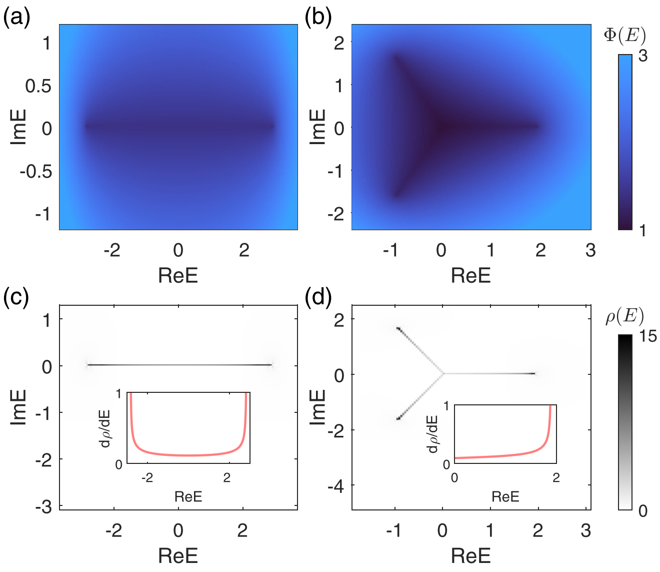

FIG. 2. Potential landscape on the complex plane associated with Hamiltonian (a) $H(\beta) = t_L\beta + t_R\beta^{-1}$ (the Hatano-Nelson model) and (b) $H(\beta) = \beta^2 + \beta^{-1}$. (c), (d) The DOS $\rho(E)$ after taking the Laplacian of the potential functions. Inset: $\frac{d\rho}{dE}$, the DOS with respect to the arc length of the spectral graph. In the inset of (d), the branch on the real axis of the graph is selected. For (a) and (c), $t_L = 2$, $t_R = 1$.

$E \in G_H$ and dub E an n-vertex if there are n arcs emanating from it and intersecting with the circle. Thus the points on the edges (interior of the arcs) of G_H are 2-vertices and the endpoints are 1-vertices. The junctions are n-vertices with $n \geqslant 3$ [e.g., $E = 0$ in Fig. 2(d)]. Figure 3 plots the spectral graph and its associated GBZ for Hamiltonian $H(\beta) = \beta^{-3} + 0.99\beta^{-2} + 0.1\beta^2 - 0.44\beta^3$. The graph $G_H = G(7, 7)$ contains two 3-vertices, one 4-vertex, and four endpoints due to the existence of a closed loop.

Different types of vertices have distinct projections onto the GBZ. As per the potential theory, for any point $E \in G_H$, the "middle" two solutions of the ChP share an equal modulus

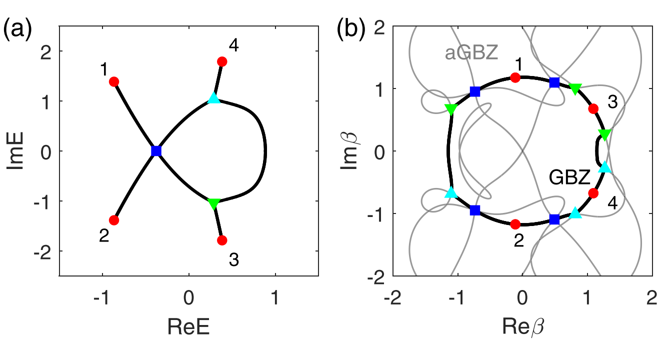

FIG. 3. Euler-graph topology associated with Hamiltonian $H(\beta) = \beta^{-3} + 0.99\beta^{-2} + 0.1\beta^2 - 0.44\beta^3$. (a) The graph $G(7, 7)$ formed by the continuum of the non-Bloch band, with four endpoints (red dots), one 4-vertex (blue square), and two 3-vertices (green and cyan triangles). (b) The GBZ (black) and auxiliary GBZ curves (gray) on the β plane. The projections of the endpoints and junction points in (a) are displayed in the same markers/colors.

$|\beta_p(E)| = |\beta_{p+1}(E)|$. When one travels around the GBZ, any arc within the graph G_H must be traversed in both directions. Consequently, the projections of a normal 2-vertex onto GBZ manifest as two separate points of the same modulus. The endpoint corresponds to the scenario of degenerate roots $\beta_p(E) = \beta_{p+1}(E)$, obeying

$$f_{\text{Res}} \equiv \text{Res}_\beta[\beta^p f(E, \beta), \partial_\beta(\beta^p f(E, \beta))] = 0, \quad (6)$$

with Res the resultant function [47,58,60–62] to discriminate degenerate solutions of the ChP. The junction point, or n-vertex ($n \geqslant 3$), has n separate projections onto the GBZ. Analytically, the junction point E has n successive β solutions of the same modulus [63]. Each projection lies at the crossing between the algebraic curves of the auxiliary GBZ (aGBZ) [14], e.g., the projections in Fig. 3(b) of the 3- or 4-vertex. It is important to note that there may exist some spurious junctions on the graph arising from spectral self-crossings, as exemplified in Fig. 4(c3). In such instances, the GBZ loop displays self-intersections and the fake junction should be treated as a normal 2-vertex on the spectral arc.

Graph transitions. The graph geometry enables uncharted spectral-graph transitions without any Hermitian analog. Unlike the band-touching-induced topological transitions responsible for the appearance of edge states, graph transitions may occur even in single-band non-Hermitian systems. Guided by the Euler formula, these transitions involve changes in the counts of vertices, edges, or faces adhering to the condition $\delta n_V - \delta n_E + \delta n_F = 0$. Given the diversity of spectral graphs, there exists an infinite array of graph transitions, which can be further broken down into more elementary ones. In the following, we pinpoint three fundamental graph transitions with concrete examples.

(i) UVY transition. Model: $H(\beta) = \beta + \alpha/\beta + 1/\beta^2$ with a tunable parameter α. As shown in Figs. 4(a1)–4(a3), the number of endpoints changes by one, $G(2, 1) \to G(4, 3)$. Initially, at $\alpha = -1.2$, there is a smooth U-turn in the arc. As α increases, the U-turn becomes narrower and sharper to develop a cusp at $\alpha = -1$. After that, a new endpoint emerges, and the graph becomes Y shaped with three arcs joined at a 3-vertex. Figures 4(a4)–4(a6) plot the GBZ. At the transition, two aGBZ curves touch.

(ii) $\mathcal{PT}$-like transition. Model: same as above, but with α varying from 4 to 2. As shown in Figs. 4(b1)–4(b3), the number of vertices and edges change by $\delta n_V = \delta n_E = 2$ with $G(2, 1) \to G(4, 3)$, accompanied by the appearance of a 3-vertex. Note that the two new branches may also emerge from the interior of the spectral arc [64], rather than at the endpoint. This is a generalization of non-Bloch $\mathcal{PT}$ breaking, where the spectra transition from real to complex, or vice versa. Similar to the former case, two aGBZ curves touch at the transition with $\alpha = 3$, as depicted in Fig. 4(b5).

(iii) Self-crossing transition. Model: $H(\beta) = \beta^3 + 2\beta^2 + \alpha\beta + 1/\beta$, with α varying from 3.2 to 2.8. In this case, the number of endpoints stays unchanged, but new junction points and spectral loops emerge. As depicted in Figs. 4(c1)–4(c3), the initial graph $G(2, 1)$ transforms into an "airplane" graph $G(3, 3)$. Due to the appearance of an additional spectral loop, $\delta n_F = 1$. Note that the 4-vertex on the right side [cyan dot in Fig. 4(c3)] is spurious as it maps onto two (rather than four) solutions on the GBZ [Fig. 4(c6)]. Nonetheless, when

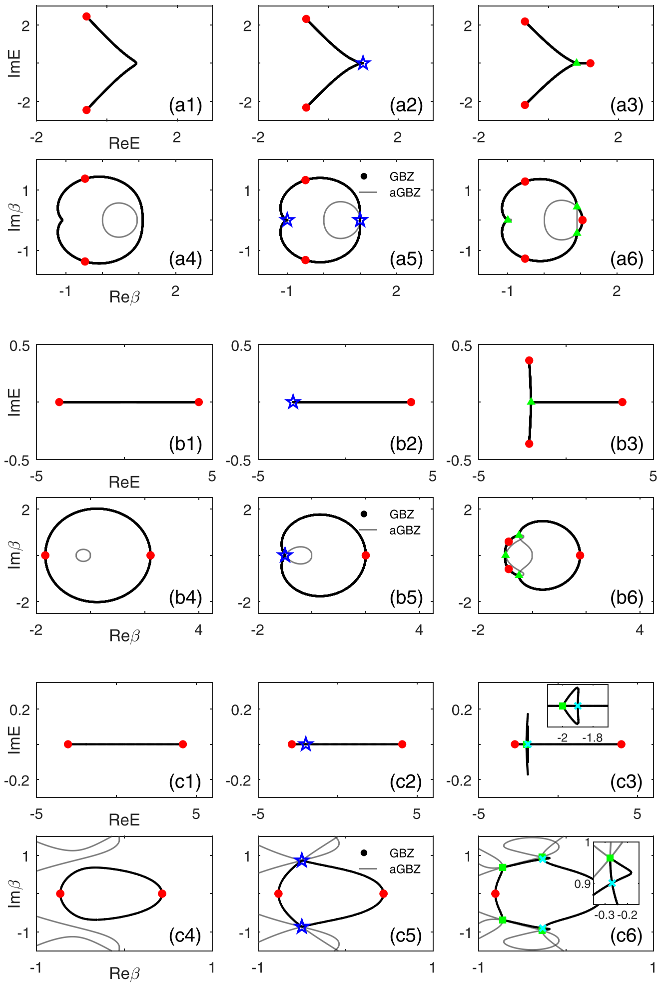

FIG. 4. Three elementary spectral-graph transitions. (a1)–(a6) UVY transition. (b1)–(b6) $\mathcal{PT}$-like transition. (c1)–(c6) Self-crossing transition. For each type, the first and second row denotes the evolutions of the spectral graph and its corresponding GBZ, respectively. The endpoints, junction points, and the spectral singularities at the transitions are marked in red, green, and blue, respectively. In (c3), the spurious 4-vertex is marked in cyan. For (a1)–(a6), from left to right, $\alpha = -1.2, -1, -0.8$. For (b1)–(b6), from left to right, $\alpha = 4, 3, 2$. For (c1)–(c6), from left to right, $\alpha = 3.2, 3, 2.8$.

traversing the GBZ, it is passed through four times. This spectral loop spans from the intermediate endpoint at $E = -2$ with $\alpha = 3$. Still, the aGBZ curves touch at the transition, resulting in the GBZ's self-crossings afterward.

We remark that all three types of transitions involve the emergent singularities in the GBZ. In the UVY/$\mathcal{PT}$-like transitions, the number of endpoints changes, which can be identified by solving all the endpoints via Eq. (6), while for the $\mathcal{PT}$-like/self-crossing transitions, there exist two coincident endpoints as shown in Figs. 4(b2) and 4(c2). Similar to the criterion of identifying the non-Bloch $\mathcal{PT}$ transition [64], the spectral transition satisfies the condition

$$\mathrm{Res}_E[f_{\mathrm{Res}}(E, \alpha), \partial_E f_{\mathrm{Res}}(E, \alpha)] = 0. \tag{7}$$

Isolated edge states. In realistic systems, isolated topological edge states may exist outside the graph. Consider a generic m-band ($m \geqslant 2$) Hamiltonian $H(\beta) = \sum_{j=-s}^{t} h_j \beta^j$ with h_j being $m \times m$ matrices and $s(t)$ the hopping range to the right (left). To accommodate the edge state $E \notin G_H$, we define an $ms \times ms$ matrix M_{edge}, with its μth row and νth column ($\mu, \nu = 1, 2, \dots, s$) an $m \times m$ block, given by

$$[M_{\mathrm{edge}}]_{\mu\nu} = \frac{1}{2\pi i}\int_{\Gamma} \beta^{\mu-\nu}[H(\beta) - E\, I_{m\times m}]^{-1}\frac{d\beta}{\beta}. \tag{8}$$

Here, $I_{m\times m}$ is the identity matrix. The line integral is defined entrywise, tracing a counterclockwise closed curve Γ which encloses the origin and the first p β solutions of $f(E, \beta) = 0$. Isolated edge modes are identified by the condition $\det M_{\mathrm{edge}} = 0$ [65]. For instance, in the nonreciprocal Su-Schrieffer-Heeger (SSH) model [8], $H(k) = (t_1 + t_2\cos k)\sigma_x + (t_2 \sin k + i\frac{\gamma}{2})\sigma_y$, $m = 2$, $s = p = 1$. It is easy to show $\det M_{\mathrm{edge}} \neq 0$ if $E \neq 0$. The admissible edge states manifest as zero modes when $|t_1^2 - \gamma^2/4| < t_2^2$ [58]. It is the topological regime indexed by a nonzero winding number [8] over the GBZ. The edge matrix is powerful in analyzing isolated edge states, including nonzero edge modes [58] without the need of bulk-invariant calculations.

Conclusion and discussion. To conclude, our study systematically delves into the geometric and topological aspects of spectral graphs of non-Hermitian non-Bloch bands, within a purely algebraic framework. Facilitated by the local form of the potential function, we unveil the electrostatic mechanism of spectral collapse, reproduce the non-Bloch band theory as well as the GBZ, and extract the spectral graph from the potential landscape. By analyzing the Euler-graph topology, we further identify three elementary spectral transitions beyond the gap-closure paradigm and address how to account for isolated edge states outside the continuum of non-Bloch bands.

The local potential function plays a vital role in bridging the graph topology of non-Hermitian non-Bloch bands with the underlying algebraic structures of the ChP. While the spectral graph is immediately derived from the potential landscape or the intersection in Eq. (2), it can also be obtained by locating self-crossing points on the rescaled spectral loops [63], or through the auxiliary GBZ method [14]. We note that the local potential formalism can also capture the spectral properties of the critical NHSE [58,66]. In contrast to the traditional wisdom of computing energy spectra for a given Hamiltonian, a reverse band-engineering strategy can be employed [44] to design tailored tight-binding Hamiltonians for a specific spectral graph. Notably, the potential landscape in our work differs from the inverse skin-depth landscape therein. Lastly, we remark that with the rapid advancements in platforms such as metamaterials [20], optics/photonics [22,24], ultracold atoms [25], and electrical networks [21,23], it is promising to customize desired non-Hermitian Hamiltonians and to identify the spectral graph transitions experimentally. For instance, the non-Bloch $\mathcal{PT}$ phase transition can be detected by extracting the Lyapunov exponents from the bulk dynamics [67,68]. This method is also applicable to some $\mathcal{PT}$-like and self-crossing types of graph transitions [58]. Additionally, we note that the spectral singularities of non-Bloch bands can be uncovered by measuring the center of mass in wave-packet dynamics [50] for ultracold atoms, serving as further signatures of the graph transitions.

Acknowledgment. This work is supported by the National Key Research and Development Program of China (Grants No. 2023YFA1406704 and No. 2022YFA1405800) and the start-up grant of IOP-CAS.

[1] C. M. Bender, Making sense of non-Hermitian Hamiltonians, Rep. Prog. Phys. **70**, 947 (2007).

[2] R. El-Ganainy, K. G. Makris, M. Khajavikhan, Z. H. Musslimani, S. Rotter, and D. N. Christodoulides, Non-Hermitian physics and PT symmetry, Nat. Phys. **14**, 11 (2018).

[3] N. Moiseyev, *Non-Hermitian Quantum Mechanics* (Cambridge University Press, Cambridge, UK, 2011).

[4] Y. Ashida, Z. Gong, and M. Ueda, Non-Hermitian physics, Adv. Phys. **69**, 249 (2020).

[5] E. J. Bergholtz, J. C. Budich, and F. K. Kunst, Exceptional topology of non-Hermitian systems, Rev. Mod. Phys. **93**, 015005 (2021).

[6] K. Ding, C. Fang, and G. Ma, Non-Hermitian topology and exceptional-point geometries, Nat. Rev. Phys. **4**, 745 (2022).

[7] K. Yang, Z. Li, J. L. K. König, L. Rødland, M. Stålhammar, and E. J. Bergholtz, Homotopy, symmetry, and non-Hermitian band topology, arXiv:2309.14416.

[8] S. Yao and Z. Wang, Edge states and topological invariants of non-Hermitian systems, Phys. Rev. Lett. **121**, 086803 (2018).

[9] S. Yao, F. Song, and Z. Wang, Non-Hermitian Chern bands, Phys. Rev. Lett. **121**, 136802 (2018).

[10] F. K. Kunst, E. Edvardsson, J. C. Budich, and E. J. Bergholtz, Biorthogonal bulk-boundary correspondence in non-Hermitian systems, Phys. Rev. Lett. **121**, 026808 (2018).

[11] K. Yokomizo and S. Murakami, Non-Bloch band theory of non-Hermitian systems, Phys. Rev. Lett. **123**, 066404 (2019).

[12] K. Zhang, Z. Yang, and C. Fang, Correspondence between winding numbers and skin modes in non-Hermitian systems, Phys. Rev. Lett. **125**, 126402 (2020).

[13] N. Okuma, K. Kawabata, K. Shiozaki, and M. Sato, Topological origin of non-Hermitian skin effects, Phys. Rev. Lett. **124**, 086801 (2020).

[14] Z. Yang, K. Zhang, C. Fang, and J. Hu, Non-Hermitian bulk-boundary correspondence and auxiliary generalized Brillouin zone theory, Phys. Rev. Lett. **125**, 226402 (2020).

[15] V. M. Martinez Alvarez, J. E. Barrios Vargas, and L. E. F. F. Torres, Non-Hermitian robust edge states in one dimension: Anomalous localization and eigenspace condensation at exceptional points, Phys. Rev. B **97**, 121401(R) (2018).

[16] C. H. Lee and R. Thomale, Anatomy of skin modes and topology in non-Hermitian systems, Phys. Rev. B **99**, 201103(R) (2019).

[17] K. Kawabata, N. Okuma, and M. Sato, Non-Bloch band theory of non-Hermitian Hamiltonians in the symplectic class, Phys. Rev. B **101**, 195147 (2020).

[18] Y. Yi and Z. Yang, Non-Hermitian skin modes induced by on-site dissipations and chiral tunneling effect, Phys. Rev. Lett. **125**, 186802 (2020).

[19] X. Zhang, T. Zhang, M.-H. Lu, and Y.-F. Chen, A review on non-Hermitian skin effect, Adv. Phys.: X **7**, 2109431 (2022).

[20] A. Ghatak, M. Brandenbourger, J. van Wezel, and C. Coulais, Observation of non-Hermitian topology and its bulk-edge correspondence in an active mechanical metamaterial, Proc. Natl. Acad. Sci. USA **117**, 29561 (2020).

[21] T. Helbig, T. Hofmann, S. Imhof, M. Abdelghany, T. Kiessling, L. Molenkamp, C. Lee, A. Szameit, M. Greiter, and R. Thomale, Generalized bulk–boundary correspondence in non-Hermitian topolectrical circuits, Nat. Phys. **16**, 747 (2020).

[22] L. Xiao, T. Deng, K. Wang, G. Zhu, Z. Wang, W. Yi, and P. Xue, Non-Hermitian bulk–boundary correspondence in quantum dynamics, Nat. Phys. **16**, 761 (2020).

[23] T. Hofmann, T. Helbig, F. Schindler, N. Salgo, M. Brzezińska, M. Greiter, T. Kiessling, D. Wolf, A. Vollhardt, A. Kabaši *et al.*, Reciprocal skin effect and its realization in a topolectrical circuit, Phys. Rev. Res. **2**, 023265 (2020).

[24] X. Zhu, H. Wang, S. K. Gupta, H. Zhang, B. Xie, M. Lu, and Y. Chen, Photonic non-Hermitian skin effect and non-Bloch bulk-boundary correspondence, Phys. Rev. Res. **2**, 013280 (2020).

[25] Q. Liang, D. Xie, Z. Dong, H. Li, H. Li, B. Gadway, W. Yi, and B. Yan, Dynamic signatures of non-Hermitian skin effect and topology in ultracold atoms, Phys. Rev. Lett. **129**, 070401 (2022).

[26] Z. Gong, Y. Ashida, K. Kawabata, K. Takasan, S. Higashikawa, and M. Ueda, Topological phases of non-Hermitian systems, Phys. Rev. X **8**, 031079 (2018).

[27] K. Kawabata, K. Shiozaki, M. Ueda, and M. Sato, Symmetry and topology in non-Hermitian physics, Phys. Rev. X **9**, 041015 (2019).

[28] H. Zhou and J. Y. Lee, Periodic table for topological bands with non-Hermitian symmetries, Phys. Rev. B **99**, 235112 (2019).

[29] C.-H. Liu and S. Chen, Topological classification of defects in non-Hermitian systems, Phys. Rev. B **100**, 144106 (2019).

[30] C.-H. Liu, H. Jiang, and S. Chen, Topological classification of non-Hermitian systems with reflection symmetry, Phys. Rev. B **99**, 125103 (2019).

[31] C. C. Wojcik, X.-Q. Sun, T. Bzdušek, and S. Fan, Homotopy characterization of non-Hermitian Hamiltonians, Phys. Rev. B **101**, 205417 (2020).

[32] Z. Li and R. S. K. Mong, Homotopical characterization of non-Hermitian band structures, Phys. Rev. B **103**, 155129 (2021).

[33] H. Hu and E. Zhao, Knots and non-Hermitian Bloch bands, Phys. Rev. Lett. **126**, 010401 (2021).

[34] C.-X. Guo, S. Chen, K. Ding, and H. Hu, Exceptional non-Abelian topology in multiband non-Hermitian systems, Phys. Rev. Lett. **130**, 157201 (2023).

[35] K. Wang, A. Dutt, C. C. Wojcik, and S. Fan, Topological complex-energy braiding of non-Hermitian bands, Nature (London) **598**, 59 (2021).

[36] Y. Yu, L.-W. Yu, W. Zhang, H. Zhang, X. Ouyang, Y. Liu, D.-L. Deng, and L.-M. Duan, Experimental unsupervised learning of non-Hermitian knotted phases with solid-state spins, npj Quantum Inf. **8**, 116 (2022).

[37] H. Hu, S. Sun, and S. Chen, Knot topology of exceptional point and non-Hermitian no-go theorem, Phys. Rev. Res. **4**, L022064 (2022).

[38] Q. Zhang, Y. Li, H. Sun, X. Liu, L. Zhao, X. Feng, X. Fan, and C. Qiu, Observation of acoustic non-Hermitian Bloch braids and associated topological phase transitions, Phys. Rev. Lett. **130**, 017201 (2023).

[39] Q. Zhang, L. Zhao, X. Liu, X. Feng, L. Xiong, W. Wu, and C. Qiu, Experimental characterization of three-band braid relations in non-Hermitian acoustic lattices, Phys. Rev. Res. **5**, L022050 (2023).

[40] M.-M. Cao, K. Li, W.-D. Zhao, W.-X. Guo, B.-X. Qi, X.-Y. Chang, Z.-C. Zhou, Y. Xu, and L.-M. Duan, Probing complex-energy topology via non-Hermitian absorption spectroscopy in a trapped ion simulator, Phys. Rev. Lett. **130**, 163001 (2023).

[41] Y. Wu, Y. Wang, X. Ye, W. Liu, C.-K. Duan, Y. Wang, X. Rong, and J. Du, Observation of the knot topology of non-Hermitian systems in a single spin, Phys. Rev. A **108**, 052409 (2023).

[42] T. Tai and C. H. Lee, Zoology of non-Hermitian spectra and their graph topology, Phys. Rev. B **107**, L220301 (2023).

[43] C. H. Lee, L. Li, R. Thomale, and J. Gong, Unraveling non-Hermitian pumping: Emergent spectral singularities and anomalous responses, Phys. Rev. B **102**, 085151 (2020).

[44] R. Yang, J. W. Tan, T. Tai, J. M. Koh, L. Li, S. Longhi, and C. H. Lee, Designing non-Hermitian real spectra through electrostatics, Sci. Bull. **67**, 1865 (2022).

[45] H.-Y. Wang, F. Song, and Z. Wang, Amoeba formulation of the non-Hermitian skin effect in higher dimensions, arXiv:2212.11743.

[46] H. Shen, B. Zhen, and L. Fu, Topological band theory for non-Hermitian Hamiltonians, Phys. Rev. Lett. **120**, 146402 (2018).

[47] Z. Yang, A. P. Schnyder, J. Hu, and C.-K. Chiu, Fermion doubling theorems in two-dimensional non-Hermitian systems for Fermi points and exceptional points, Phys. Rev. Lett. **126**, 086401 (2021).

[48] L. Xiao, T. Deng, K. Wang, Z. Wang, W. Yi, and P. Xue, Observation of non-Bloch parity-time symmetry and exceptional points, Phys. Rev. Lett. **126**, 230402 (2021).

[49] F. Song, H.-Y. Wang, and Z. Wang, Non-Bloch PT symmetry: Universal threshold and dimensional surprise, in *A Festschrift in Honor of the CN Yang Centenary: Scientific Papers* (World Scientific, Singapore, 2022), pp. 299–311.

[50] F. Qin, R. Shen, L. Li, and C. H. Lee, Kinked linear response from non-Hermitian pumping, arXiv:2306.13139.

[51] N. Hatano and D. R. Nelson, Localization transitions in non-Hermitian quantum mechanics, Phys. Rev. Lett. **77**, 570 (1996).

[52] H. Hu, Non-Hermitian band theory in all dimensions: uniform spectra and skin effect, arXiv:2306.12022.

[53] A. Böttcher and S. M. Grudsky, *Spectral Properties of Banded Toeplitz Matrices* (SIAM, Philadelphia, 2005).

[54] Exceptions do exist, e.g., when the graph consists of only a few points.

[55] J. L. Ullman, A problem of Schmidt and Spitzer, Bull. Amer. Math. Soc. **73**, 883 (1967).

[56] G. Szegö, Ein Grenzwertsatz über die Toeplitzschen Determinanten einer reellen positiven Funktion, Math. Ann. **76**, 490 (1915).

[57] G. Szegö, On certain Hermitian forms associated with the Fourier series of a positive function, Comm. Sém. Math. Univ. Lund [Medd. Lunds Univ. Mat. Sem.] **1952**, 228 (1952).

[58] See Supplemental Material at http://link.aps.org/supplemental/10.1103/PhysRevB.109.L100301 for more details on (I) the derivation of the local spectral potential; (II) the linear DOS of the Hatano-Nelson model and the "fan" model; (III) application to critical non-Hermitian skin effect; (IV) the resultant function; (V) calculations of isolated topological edge modes outside the spectral graph; and (VI) bulk dynamics as a probe to the graph transitions.

[59] If the spectral graph has n_C components, the right side of the Euler formula should be modified to be $1 + n_C$.

[60] H. Woody, Polynomial resultants, GNU operating system (2016), http://buzzard.ups.edu/courses/2016spring/projects/woody-resultants-ups-434-2016.pdf.

[61] S. Janson, Resultant and discriminant of polynomials, Notes, September 22 (2007), https://www2.math.uu.se/~svante/papers/sjN5.pdf.

[62] I. M. Gelfand, M. M. Kapranov, and A. V. Zelevinsky, *Discriminants, Resultants, and Multidimensional Determinants* (Birkhäuser, Boston, 1994).

[63] D. Wu, J. Xie, Y. Zhou, and J. An, Connections between the open-boundary spectrum and the generalized Brillouin zone in non-Hermitian systems, Phys. Rev. B **105**, 045422 (2022).

[64] Y.-M. Hu, H.-Y. Wang, Z. Wang, and F. Song, Geometric origin of non-Bloch *PT* symmetry breaking, Phys. Rev. Lett. **132**, 050402 (2024).

[65] S. Delvaux, Equilibrium problem for the eigenvalues of banded block Toeplitz matrices, Math. Nachr. **285**, 1935 (2012).

[66] L. Li, C. H. Lee, S. Mu, and J. Gong, Critical non-Hermitian skin effect, Nat. Commun. **11**, 5491 (2020).

[67] S. Longhi, Probing non-Hermitian skin effect and non-Bloch phase transitions, Phys. Rev. Res. **1**, 023013 (2019).

[68] S. Longhi, Non-Bloch $\mathcal{PT}$ symmetry breaking in non-Hermitian photonic quantum walks, Opt. Lett. **44**, 5804 (2019).